Scalable Electrochemical Surface Enhanced Raman Spectroscopy (EC-SERS) for bio-chemical analysis

Chuan Xiao

Thesis submitted to the faculty of the Virginia Polytechnic Institute and State University in partial fulfillment of the requirements for the degree of

Master of Science

In

Electrical Engineering

Wei Zhou

Weinan Leng

Xiaoting Jia

July 26th, 2021

Blacksburg, Virginia

Keywords: nanoimprint lithography (NIL), multi-walled carbon nanotubes (MWCNTs), carbon-nanotube doped polymeric nanocomposites, conducting nanopillar arrays, electrochemical impedance spectroscopy (EIS)

Scalable Electrochemical Surface Enhanced Raman Spectroscopy (EC-SERS) for bio-chemical analysis

Chuan Xiao

(ABSTRACT)

Conducting vertical nanopillar arrays can serve as three-dimensional nanostructured electrodes with improved performance for electrical recording and electrochemical sensing in bio-electronics applications. However, vertical nanopillar-array electrodes made of inorganic conducting materials by conventional nanofabrication approach still faces challenges in high manufacturing costs, poor scalability, and limited choice of carrier substrates. Here, we report a new type of conducting nanopillar arrays composed of multi-walled carbon nanotubes (MWCNTs) doped polymeric nanocomposites, which are manufactured over the wafer-scale on both rigid and flexible substrates by direct nanoimprinting of perfluoropolyether nanowell-array templates into uncured MWCNT/polymer mixtures. By controlling the MWCNT ratios and the annealing temperatures during the fabrication process, MWCNT/polymer nanopillar arrays can possess outstanding electrical properties with high DC conductivity (~4 S/m) and low AC electrochemical impedance (~10^4 Ω at 1000 Hz). Moreover, by electrochemical impedance spectroscopy (EIS) measurements and equivalent circuit modeling-analysis, we can decompose the overall impedance of MWCNT/polymer nanopillar arrays in the electrolyte into multiple bulk and interfacial circuit components, and thus can illustrate their different dependence on the MWCNT ratios and the annealing temperatures. In particular, we find that a proper annealing process can significantly reduce the anomalous ion diffusion impedance and improve the impedance properties of MWCNT/polymer nanopillars in the electrolyte.

Scalable Electrochemical Surface Enhanced Raman Spectroscopy (EC-SERS) for bio-chemical analysis

Chuan Xiao

(GENERAL AUDIENCE ABSTRACT)

Conducting vertical nanopillar arrays can serve as three-dimensional nanostructured electrodes with improved performance for electrical recording and electrochemical sensing in nano-bioelectronics applications. However, vertical nanopillar-array electrodes made of inorganic conducting materials by conventional nanofabrication approach still faces challenges in high manufacturing costs, poor scalability, and limited choice of carrier substrates. Compared to conventional nanofabrication approaches, nanoimprint lithography exhibits unique advantages for low-cost scalable manufacturing of nanostructures on both rigid and flexible substrates. Very few studies, however, have been conducted to achieve the scalable nanoimprinting fabrication of conducting nanopillar arrays made of MWCNT/polymer nanocomposites.

Here, we report a new type of conducting nanopillar arrays composed of multi-walled carbon nanotubes (MWCNTs) doped polymeric nanocomposites, which can be manufactured over the wafer-scale on both rigid and flexible substrates by direct nanoimprinting of the perfluoropolyether nanowell-array template into uncured MWCNT/polymer mixtures. We find that the nanoimprinted conducting nanopillar arrays can possess appealing electrical properties with a high DC conductivity (~4 S/m) and a low AC electrochemical impedance (~10^4 Ω at 1000 Hz) in the physiologically relevant electrolyte solutions (1X PBS). Furthermore, we conduct a systematic equivalent circuit modeling analysis of measured EIS results to understand the effects of the MWCNT ratios and the annealing temperatures on the impedance of different bulk and interfacial circuit components for MWCNT/polymer nanopillar arrays in the electrolyte.

Acknowledgments

Throughout my graduate studies, I had the pleasure of working with fantastic people at Virginia Tech who supported me. First, I want to thank my supervisor, Professor Wei Zhou. He taught me how to design the experiment from scratch and he has inspired me always to be the best person I can be. I would also like to acknowledge my excellent lab mates from Dr. Wei Zhou's group. I would like to single out my collaborator Yuming Zhao. Yuming contribute a lot on the Electrochemical analysis of my system.

ATTRIBUTION

Wei Zhou and Chuan Xiao conceived of the present idea. Chuan Xiao planned and carried out the experiment. Wei Zhou helped and advised on experiment planning and outline. Chuan Xiao contribute to the sample preparation and characterization results. Chuan Xiao and Yuming Zhao contribute to the interpretation of the results.

Professor Wei Zhou, my supervisor of my Master of science program at Virginia Tech.

Yuming Zhao, my lab mate in Dr. Zhou's research group.

Contents

List of Figures

List of Tables

Chapter 1

1. Introduction & literature review

1.1 Motivation

Three-dimensional nanostructured electrodes based on conducting vertical nanopillar arrays have emerged as a useful tool in nano-bioelectronics for electrical recording of extracellular and intracellular membrane potentials[1-5] as well as electrochemical sensing.[6-9] Furthermore, recent studies have shown that living cells can engulf vertical nanopillar electrodes with a tight adhesion to improve electrical coupling at the cell-nanodevice interface.[10, 11] Also, dense arrays of nanopillar electrodes can be integrated with large-scale circuits to perform the parallel electrical recording over the cellular network.[12] In most previous works, vertical nanopillar-array electrodes are made of inorganic conducting materials (e.g., Si, Au, and Pt) by conventional nanofabrication techniques using electron-beam lithography and focused ion beam milling, which faces difficulties in high manufacturing costs, poor scalability, and limited choice of carrier substrates. Compared to conventional nanofabrication approaches, nanoimprint lithography exhibits unique advantages for low-cost scalable manufacturing of nanostructures on both rigid and flexible substrates.[13-15] Very few studies, however, have been conducted to achieve the scalable nanoimprinting fabrication of conducting nanopillar arrays made of MWCNT/polymer nanocomposites, which potentially can feature appealing properties in terms of combined mechanical flexibility and strength as well as good (bio-)chemical stability and solvent resistance.[16-22]

1.2 Research results

In this work, we demonstrate the scalable nanoimprinting fabrication of conducting MWCNT/polymer nanopillar arrays, which can possess high DC conductivity (~4 S/m) and low AC electrochemical impedance (~10^4 Ω at 1000 Hz). In particular, wafer-scale conducting MWCNT/polymer nanopillar arrays can be manufactured by direct nanoimprinting of perfluoropolyether (PFPE) nanowell-array templates with high stiffness into uncured MWCNT/polymer mixtures. After the curing process, the hydrophobic PFPE nanowell-array templates can be separated from imprinted MWCNT/polymer nanopillar arrays. From 2D Raman mapping measurements, we observe that the distributions of MWCNTs are uniform on the scale of ~25 × 25

m^2 but random in the sub-micrometer scale. Furthermore, we conduct 4-point probe DC conductivity measurements and AC electrochemical impedance spectroscopy (EIS) to investigate the effects of the MWCNT ratios and the annealing temperatures on the electrical properties of MWCNT/polymer nanopillar arrays. By an equivalent circuit modeling and analysis, we can decompose the contributions to the overall EIS behaviors from different bulk and interfacial circuit elements, and we reveal that the anomalous ion diffusion processes play a significant role in determining the EIS properties of MWCNT/polymer nanopillar arrays in the electrolyte.

Chapter 2

2. Experiments

2.1 Materials and chemicals

Carboxyl functionalized MWCNTs with a diameter of 10-20nm and length of 20-30um (purity>95 wt%) were purchased from Cheap Tubes Inc., USA. The UV-curable polymer NOA83H, also containing the thermal curing catalyst, was supplied by Norland Product Inc., (USA). Sylgard-184 PDMS (Dow corning) was obtained from Ellsworth Adhesives (USA). PFPE Fluorolink MD 700 was purchased from Solvay S.A. (Belgium). Photoinitiator 2-Hydroxy-2-methylpropiophenone was obtained from Sigma-Aldrich (USA). The Silicon 3" P (100) 0-100 ohm-cm SSP 406-480um Test Grade wafer was supplied by UniversityWafer Inc. (USA). (TRIDECAFLUORO-1,1,2,2-TETRAHYDROOCTYL)-1-TRI (TFCOS) was obtained from UCT Specialties (USA).

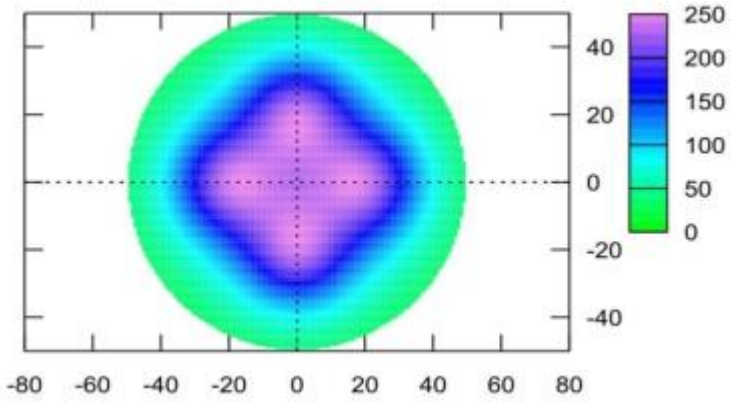

Figure S-1. The power distribution in mW/cm2 of CNI from NIL technics.

2.2 Fabrication of MWCNT/polymer nanopillar arrays

2.2.1 Preparation of uncured MWCNT/NOA83H mixtures

The uncured MWCNT/NOA83H mixtures were created by mixing uncured NOA83H polymer with MWCNT nanofillers at controlled weight percentages using a homogenizer (Fisher Scientific, PowerGen 1000). Mixtures of uncured MWCNT/NOA83H were homogenized by 5 repeating cycles for 1 min at 6000 rpm followed by 1 min rest. We applied 1 min rest between repeating homogenization cycles to alleviate the heating accumulation due to the continuous homogenization process and avoid the undesired partial curing of NOA83H.

2.2.2 Fabrication of polyurethane (PU) nanopillar-array template

As shown in Figure 1A, PU nanopillar-array templates were created by the nanoimprinting with a PDMS nanowell-array stamp, which was duplicated from a silicon master consisting of a 2D square periodic arrays of Si nanopillars (periodicity: 400 nm, diameter: ~100 nm, and height: ~400 nm).[23] We conducted the imprint process with a desktop Compact Imprinting tool (CNI, NIL Technology ApS, Denmark). After dropping 2-3 drops of NOA83H on the PET film (thickness: ~300 m), the PDMS nanowell-array template was gently placed on the NOA83H droplet to imprint the NOA83H into nanopillar arrays by UV exposure for 5 min (50% of power, Fig. S-1, †) under 0 bar pressure. A 6-hour post-baking process at 80˚C in the oven was applied to cure the NOA83H-based PU nanopillar-array template fully.

2.2.3 Fabrication of perfluoropolyether (PFPE) nanowell-array template

PFPE nanowell-array templates were fabricated by nanoimprinting with the TFOCS treated PU nanopillar-array templates (Fig. 1A). After an oxygen plasma surface modification of the PU nanopillar-array templates, the TFOCS treatment was performed in a desiccator for 30 min under the vacuum condition to make a hydrophobic surface for the PU nanopillar-array templates. The TFOCS treatment of the PU nanopillar arrays will slightly increase their diameter (~10-15nm on the side) and height (~30nm) of the nanopillars due to the added TFOCS coating layers (AFM results not shown here).[24] Next, we placed 2-3 drops of PFPE with 4 wt% photoinitiator on the PET film. After placing PU nanopillar-array template on the PFPE droplet, we loaded the template-PFPE-PET sandwich structures the CNI nanoimprinting tool for 2 min under 0.5 bar

pressure and then conducted UV curing (50% of power) for 3 min under 0.5 bar pressure. After peeling off the PU template, we applied the additional UV exposure (50% of power) for 10 min to cure PFPE nanowell arrays in a vacuum (<10 mbar) condition with suppressed oxygen inhibition of curing processes.

CNT ratio	Imprinting pressure (bar)
0%	0
5%	0.3
10%	0.5
20%	1
30%	2

Table S-1. The pressure used for different MWCNT ratio

2.2.4 Fabrication of MWCNT/polymer nanopillar arrays

We used the PFPE nanowell-array template to imprint uncured MWCNT/NOA83H mixtures (Fig. 1A) and created conducting nanopillar arrays on both rigid Si substrates (Fig. 1B) and flexible PET films (Fig. 1C). Briefly, Si and PET substrates were cleaned by acetone and IPA rinsing. After drying by nitrogen flow, we performed the oxygen plasma treatment to make substrate surface hydrophilic in a reactive ion etching system (RIE-1C, Samco, Japan) with the oxygen flow of 20 sccm and the RF power of 50 W for 30 sec. Next, we placed 2 to 3 drops of uncured MWCNT/NOA83H mixtures on the substrates for the nanoimprinting process. Notably, when the MWCNT filling ratio is above 10 wt%, uncured MWCNT/NOA83H mixtures have a high viscosity to prevent a uniform spreading during the imprinting process. To address this issue, we used a blade to evenly spread MWCNT/NOA83H mixtures on the substrates before imprinting. After gently placing the PFPE nanohole-array template on the uncured MWCNT/NOA83H layer, we carried out the imprinting process under proper pressures (Table. S-1, †) for ~2 min and then applied UV curing (50% of power) for ~10 min with the same pressure. After the imprinting process, we performed an extra thermal curing process of

imprinted MWCNT/NOA83H mixtures in the oven with 130 ˚C for ~150 min.

2.3 Characterization of MWCNT/polymer nanopillar arrays

2.3.1 Raman spectroscopy measurement

We conducted Raman spectroscopy measurements to characterize the distributions of MWCNTs in the fabricated conducting nanopillar-arrays made of MWCNT/polymer composites. A confocal Raman microscope (Alpha 300RS, WItec, Germany) was used to collect Raman signals from 25 × 25 pixels over a 25 × 25 m^2 area using a 20X objective lens under 785nm laser excitation (2 mW) with an integration time of 1 s per pixel. The backscattered photons were detected by a spectrometer (UHTS300, WItec, Germany) equipped with a CCD camera (DU401A, Oxford Instruments, UK). After the signal acquisition, cosmic ray removal and baseline correction were performed using the software (Project v4.1, WITec, Germany).

2.3.2 Four-point probes conductivity characterization

We measured the surface conductivity of samples using a tabletop four-point probe system (Pro4-440N, Sagnatone, USA). We used a four-point resistivity probing head to control the probe-sample interface. The probing head has four probing tips with a radius of 0.04 mm and a tip-to-tip distance of 1.6 mm and uses a pressure of 85 grams during the measurement. For each type of sample, we measured surface conductivity in a total number of 20 points from 4 different locations by applying five different voltages. We characterized the thicknesses of the MWCNT/NOA83H composite layers with nanopillar arrays by a profiler (DektakXT, Bruker Corporation, USA), which shows an average thickness of about 40 m. The conductivity was calculated using the expression:[25]

$$\sigma = \frac{1}{g} \cdot \frac{1}{h} \cdot \frac{V}{I} \quad (1),$$

where t is the thickness of the conducting thin film, V is the applied voltage, I is the measured current, and g is the correction factor depending on the geometric parameters in the measurements. In the four-point probe measurements of our samples, the distance s between neighboring probes is 0.159 cm, and the thickness h of imprinted MWCNT/polymer nanopillar array samples is around 40 m. Since the ratiometric value of h/s

(0.0252) is much smaller than 1, the samples can be considered as thin films in the measurements. Considering the distance of the measured position to the nearest boundary was larger than 5 • *s* (~ 0.8 cm), a correction factor *g* of 4.53 was used to calculate the conductivity.[25]

2.3.3 Electrochemical Impedance Spectroscopy

We carried out electrochemical impedance spectroscopy (EIS) measurements of conducting nanopillar-array samples between 1 Hz and 100k Hz (10 mV, 10 points per decade) using a portable potentiostat (SP-150, Bio-logic Science Instrument, USA). The conducting nanopillar-array samples served as the working electrodes and electrically connected to the potentiostat via the silver paint and copper wires, which were physically fixed to the surface of conducting nanopillar arrays by the epoxy. PDMS chambers with a 0.5 cm diameter opening were glued with nanopillar-array samples to create electrochemical cells for the EIS measurements with well-defined surface areas of working electrodes. We used a reference electrode (Harvard Apparatus 690023, leak-free reference electrode, 2 mm, Warner Instruments, USA) and a Pt wire counter electrode (99.95% pure, 0.004'' diameters, Surepure Chemicals inc. USA) for the EIS measurements.

Chapter 3

3. Results and discussion

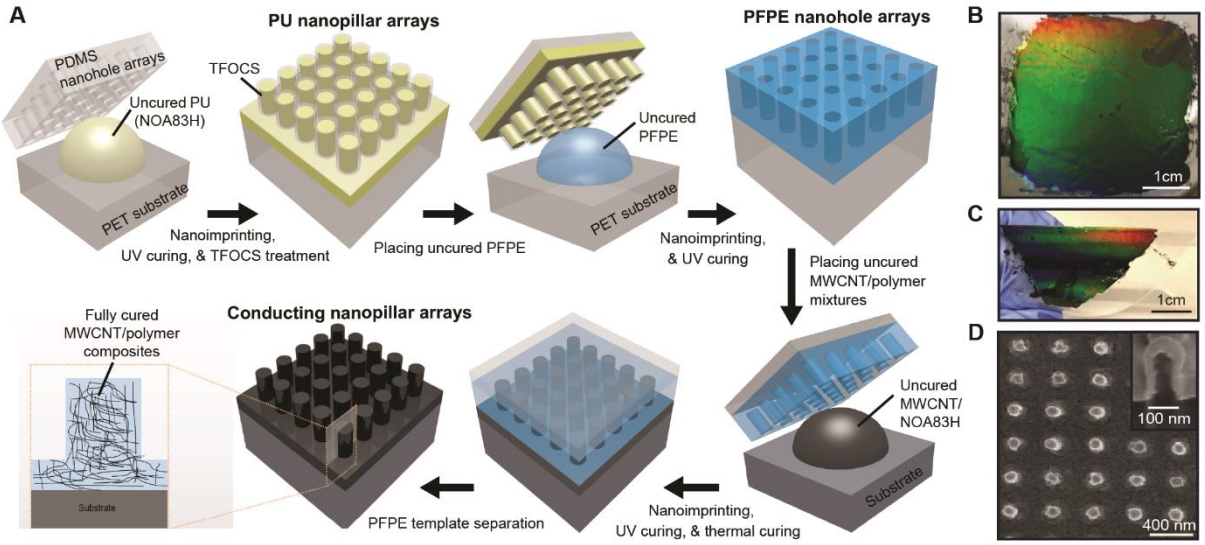

Figure 1. Nanoimprinting Conductive MWCNT/polymer nanocomposite NPAs by. (A) Schematic illustration of nanoimprinting fabrication processes to create Conductive NPAs of MWCNT/polymer composite by nanoimprinting. (B) Top-down view optical image of conductive MWCNT/polymer composite NPAs on silicon substrate. (C) Optical image of bent conductive MWCNT/polymer composite NPAs on flexible PET substrate. (D) Top view and cross-section view SEM image of conductive MWCNT/polymer composite NPAs

3.1 Fabrication of MWCNT/polymer nanopillar arrays

3.1.1 Nanoimprinting process

As shown in Figure 1A, we developed a high-throughput fabrication process to manufacture wafer-scale conducting nanopillar arrays by nanoimprinting of PFPE nanowell-array templates into uncured MWCNT/polymer mixtures on the planar substrates. With the surface-functionalized carboxyl group, the MWCNTs can achieve a good disperse quality [19] to blend with the commercially available single-component liquid optical adhesive (NOA-83H) using thiol-ene chemistry, which can allow for both UV curing and thermal curing of the MWCNT/ NOA-83H mixture. Notably, fully cured NOA 83 polymer has shown good bio-

compatibility and solvent-resistance properties for biological and chemical applications.[18, 26] We created PFPE nanowell-array templates on transparent and flexible PET sheets (thickness: ~300 m) by a two-step replication process, first from a PDMS nanowell-array stamp into a PU nanopillar-array template, and then from a PU nanopillar-array template into a PFPE nanowell-array template (details in Section 2.2). Compared to nanostructured PDMS templates typically used in the soft lithography process, nanostructured PFPE templates carried on thin PET sheets can provide several advantages for the nanoimprinting fabrication of conducting MWCNT/polymer nanopillar arrays. First, fluoro-polymer based PFPE templates are highly hydrophobic with low surface energy (~18.5 mNm-1)[17, 27], which can ensure their easy separation from imprinted MWCNT/polymer nanopillar arrays after the curing process. Second, PFPE templates have higher stiffness (Young's modulus: ~10.5 MPa) than PDMS templates (Young's modulus: ~2.05 MPa)[17, 19] to minimize the deformation of their nanoscale geometries at a high nanoimprinting pressure, which can facilitate accurate molding of nanostructures into uncured MWCNT/polymer mixtures with very high viscosity. Third, our PFPE templates carried on PET thin-sheets are highly flexible/bendable but mechanically robust, which can allow for conformal contact with substrates of the curved surface and minimize shear stress during the nanoimprinting process. Since MWCNT nanofillers can absorb UV light efficiently, we purposefully used the NOA83H, which can be cured by both UV exposure and thermal heating, to create uncured MWCNT/polymer mixtures for the nanoimprinting fabrication of conducting nanopillar arrays. In this way, we can first use the nanoimprinting tool to apply a quick UV curing (~ 10 min) to fix the imprinted nanopillar-array nanostructures in the outer layer of uncured MWCNT/polymer mixtures and then use an oven to do a thermal curing (~ 150 min) of MWCNT/polymer mixtures in the inner layer not accessible to UV light exposure for a batch of many samples. Notably, in order to prevent the oxygen inhibition effect,[28] the UV curing process was operated under the vacuum condition in the camber of the nanoimprinting tool.

3.1.2 Geometric characterization

By nanoimprinting, we successfully manufactured waferscale MWCNT/polymer nanopillar arrays over a 4cm × 4cm area on both rigid Si substrates (Figure 1B), and flexible PET polymer sheets (Figure 1C). From the camera images in Figures 1B-C, we can observe light diffraction patterns of the rainbow color over

large areas from samples, indicating a uniform distribution of periodic nanostructures on the sample surface, while the dark appearance in non-diffraction regions reveals a broadband absorption by MWCNT nanofillers at visible frequencies. Figure 1D shows the top-down and the cross-sectional (the inset of Figure 1D) scanning electron microscopy (SEM) images of the fabricated MWCNT/polymer nanopillar arrays, which consist of individual vertical nanopillars with a ~100 nm diameter and a ~250 nm height arranged in the square lattice with a 400 nm periodicity.

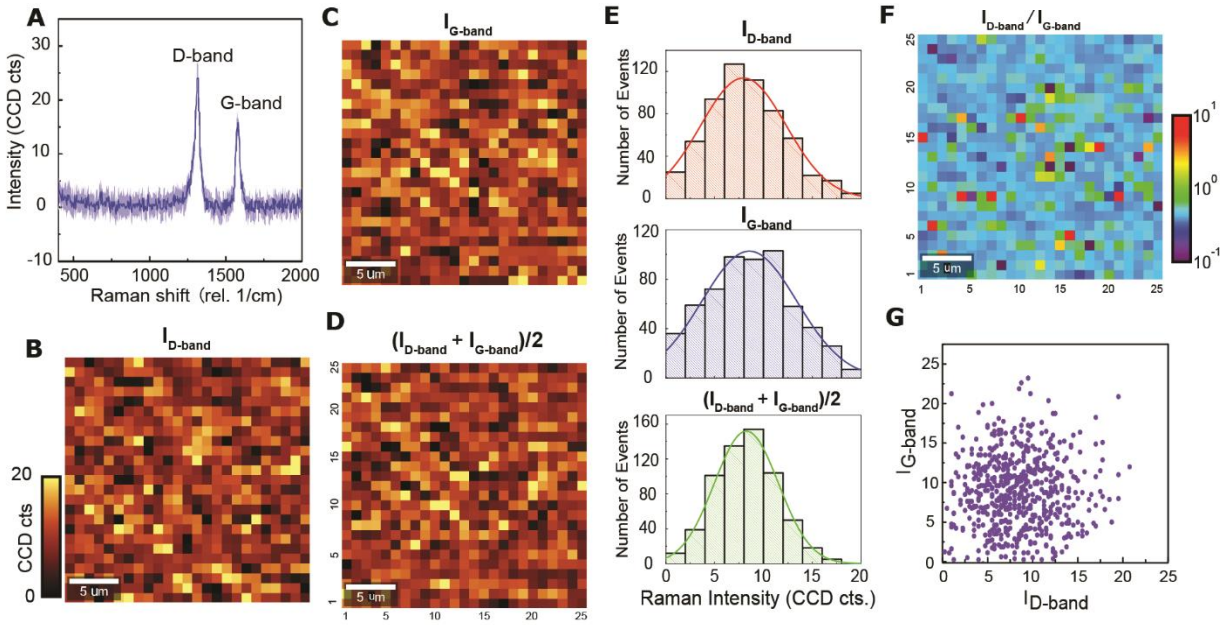

Figure 2. Raman characterization of conductive MWCNT/polymer composite NPAs. A) Raman spectra of MWCNT in polymer matrix with 25 x 25 um area under 785 nm laser excitation. (B,C,D) Scanning confocal Raman intensities images of MWCNT in polymer matrix at (B) $I_{D\text{-band}}$ (1340 cm^{-1}), (C) $I_{G\text{-band}}$ (1580 cm^{-1}), and (D) ($I_{D\text{-band}}$ + $I_{G\text{-band}}$)/2. (E) Histograms of Raman signal intensities of $I_{D\text{-band}}$, $I_{G\text{-band}}$, and ($I_{D\text{-band}}$ + $I_{G\text{-band}}$)/2. (F) Scanning confocal Raman intensities images of ratio of $I_{D\text{-band}}/I_{G\text{-band}}$. (G) The $I_{D\text{-band}}$ and $I_{G\text{-band}}$ plotting correspond to each pixel of Raman measurement.

3.1.3 Raman characterization of MWCNT distributions

To investigate the spatial distribution of MWCNTs in the polymer matrix, we performed 2D Raman spectroscopy imaging measurements for the sample of 20 wt% MWCNT/polymer nanopillar arrays under 785 nm laser excitation. As shown in Figure 2A, the average Raman spectrum from 25 × 25 pixels exhibits two distinct peaks at ~1340 cm^{-1} and ~1580 cm^{-1} with comparable values of their average peak intensity. The Raman peak at ~1340 cm^{-1} is associated with the disorder-related D-band from the sp^2-hybridized mode of carbon in MWCNTs mainly due to the detects of carboxyl functionalization groups on MWCNTs. In comparison, the peak at ~1580 cm^{-1} is the graphene-like G-band from the in-plane mode of carbon atoms in MWCNTs.[29] The 2D confocal Raman image both at D-band (Figures 2B) and G-band (Figures 2C) depicts a random distribution of Raman peak intensities without apparent spatial correlation among different pixels. Figure 2D shows the 2D mapping image of the $(I_D+I_G)/2$ by averaging both D-band and G-band Raman intensities to reflect the concentration of randomly oriented MWCNTs at each pixel. Considering the pixel size of 1 m^2 and the pixel-to-pixel distance of 1 m, the observation of a random spatial distribution of I_D, I_G, and the $(I_D+I_G)/2$ Raman intensities suggests that the mixing of MWCNT networks is not uniform at the sub-micrometer scale in the polymer matrix. Future research can explore the ways to improve the local dispersion uniformity of MWCNT networks in uncured polymer materials, such as using shorter or thinner MWCNTs to reduce the viscosity of MWCNT/polymer mixtures or optimizing the homogenizer tip geometry to improve the mechanical blending efficiency.

For statistical analysis of MWCNT spatial distributions, we plotted the histograms of I_D, I_G, and $(I_D+I_G)/2$ for 25 × 25 pixels across the 25 m × 25 m area on 20 wt% MWCNT/polymer nanopillar arrays (Figure 2E), which shows the several key points. First, the histogram plots for I_D, I_G, and $(I_D+I_G)/2$ all fit well to the normal distribution shape, reflecting that the dispersion of MWCNT is uniform on the scale of ~25 × 25 m^2 despite the significant variations of the MWCNT concentration in the sub-micrometer scale. Second, the I_G histogram shows a larger standard deviation (^{2} ~ 4.85) than the I_D histogram (^{2} ~ 4.38) since the Raman peak of in-plane graphene-like G-band in MWCNTs is more sensitive to the orientation variations for MWCNTs than the sp^2-hybridized D-band from localized defects in MWCNTs. Third, the $(I_D+I_G)/2$ histogram shows an even smaller standard deviation (^{2} ~ 3.28) by combining the Raman signals from both G-band and

D-band contributions, which thus can provide a better estimation of the local concentrations for MWCNTs of different orientations compared to I_D and I_G.

Considering that I_G from in-plane G-band is much more sensitive on NWCNT orientations than I_D from sp^2-hybridized D-band of localized defects, the spatial distribution of the ratiometric I_D/I_G values can reveal the spatial distribution of average MWCNT orientations in the polymer matrix. As shown in Figure 2F, I_D/I_G values vary widely in the range from 0.1 to 10 with a random spatial distribution, reflecting a random orientation of MWCNTs embedded in MWCNT/polymer nanopillar arrays. Figure 2G depicts the scatter plot of the relation between I_D and I_G from 25 × 25 pixels. The broad normal distribution of scatters centered near the position of (10, 10) reveals that the values of I_D and I_G from individual pixels have a relatively weak correlation of each other. Therefore, the spatial distributions of MWCNT concentrations, MWCNT defect densities, and MWCNT orientations are all random, and both I_D and I_G intensities are proportional to MWCNT concentrations.

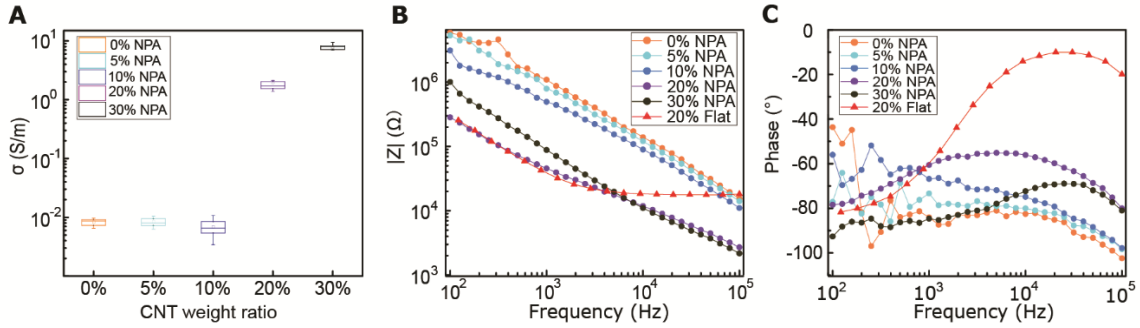

Figure 3. Conductivity and EIS characterization of different MWCNT ratio of conductive MWCNT/polymer composite. (A) Results of conductivity of 20 points per sample calculated from the sheet resistance measured by 4 point probe of different MWCNT ratio. (B,C) EIS (B) impedance and (C) phase results of different MWCNT ratio and different structure of conductive MWCNT/polymer composite from 10^2 Hz to 10^5 Hz in pH=7.4 PBS solution.

3.2 Study of MWCNT/polymer nanopillar arrays with different MWCNT filling ratios

3.2.1 Conductivity properties

Figure 3A shows the four-point probe measured conductivity properties for samples of MWCNT/polymer nanopillar arrays with different MWCNT weight ratios. As the MWCNT ratio increases

from 0 wt% to 5 wt% and 10 wt%, the conductivity does not change much and only shows small values varying between ~0.0068 S/m and ~0.0084 S/m. When the MWCNT ratio increases from 10 wt% to 20 wt%, however, the conductivity of samples significantly rises from 0.0068 S/m to 1.99 S/m by over two orders of magnitude. Thus, a percolation threshold of interconnected MWCNT networks is reached at an MWCNT weight ratio between 10 wt% and 20 wt%, similar to the previous report.[30] As the MWCNT ratio further increases from 20 wt% to 30 wt%, the conductivity of the samples increases from 1.99 to 7.79S/m due to the increased density of interconnections in MWCNT networks. The relative standard deviation values of conductivity for 5, 10, 20, 30 wt% conducting nanopillar arrays are 16.0%, 32.4%, 34.0%, and 9.1%, which can be attributed to spatial variations of MWCNT distributions in the polymer matrix shown in 2D Raman mapping measurements (Figure 2).

3.2.2 EIS properties

Figure 3B depicts the EIS measured |Z| spectra in the range between 10^2 Hz and 10^5 Hz for MWCNT/polymer nanopillar arrays with different MWCNT ratios in comparison with a reference sample of 20 wt% MWCNT/polymer flat film. For nanopillar array samples with MWCNT ratios of 0, 5 and 10 wt% below the percolation threshold, their |Z| values continuously decrease from ~3 $\times 10^6$ Ω to ~1 $\times 10^4$ Ω with increased frequency from 10^2 Hz to at 10^5 Hz. In contrast, the |Z| spectra for nanopillar array samples with 20 wt% and 30 wt% of MWCNT ratios show significantly reduced values by one order of magnitude over the entire frequency range from 10^2 Hz to 10^5 Hz. Interestingly, the 30% nanopillar array sample shows a slightly lower |Z| than that of the 20% nanopillar array sample at the higher-frequency range (10^4 - 10^5 Hz). However, at the lower-frequency range (10^2 – 10^3 Hz), the 20% nanopillar array sample has a much smaller |Z| than the 30% nanopillar array sample. For example, at 1000 Hz, |Z| for 20 wt% MWCNT/polymer nanopillar arrays is 4.5×10^4 while |Z| for 30 wt% MWCNT/polymer nanopillar arrays is 8.8×10^4 Ω. The observation of a lower impedance for the 20 wt% nanopillar array sample compared to the 30 wt% nanopillar array sample suggests that the 20 wt% nanopillar array sample may have a better dispersion quality of MWCNTs in the polymer matrix due to lower viscosity of uncured MWCNT/polymer mixtures. In contrast, a high MWCNT ratio of 30 wt% may lead to undesired MWCNT aggregations during the blending process, which can reduce the active

surface area at the interface with the electrolyte. Compared to 20 wt% MWCNT/polymer nanopillar arrays, the |Z| spectrum for the 20 wt% MWCNT/polymer flat film shows a similar shape of decreasing |Z| values with the frequency increased from ~1×10^2 Hz to ~3×10^3 Hz. However, as the frequency further increases from ~3×10^3 Hz to ~1×10^5 Hz, the |Z| values of the flat MWCNT/polymer sample starts to level off around 1.7×10^4 Ω, indicating that the impedance properties of MWCNT/polymer composites also depend on the nanostructured surface geometries.

Figure 3C shows the spectra of the impedance phase angle for different MWCNT/polymer samples. For nanopillar array samples with 0, 5 and 10 wt% MWCNT ratios, as the frequency decreases from ~10^5 Hz to ~10^3 Hz, the impedance phase angle first increases and then slowly levels off; as the frequency further decreases from ~10^3 Hz to ~10^2 Hz, the impedance phase angle starts to fluctuate significantly in a random manner due to the longer travel distance of ions at lower frequency range. For the nanopillar array with 20 wt% MWCNT ratio, as the frequency increases from ~10^2 Hz to ~10^4 Hz, the impedance phase angle increases from ~-80° to the peak value of ~-55°, and as the frequency further increases to ~10^5 Hz, the phase angle reduces to ~-81°. Unlike the 20 wt% MWCNT/polymer nanopillar arrays, 30 wt% MWCNT/polymer nanopillar arrays shows a peak impedance phase angle of ~-70° at ~2×10^4 Hz, and the flat MWCNT/polymer sample shows a peak impedance phase angle of ~-10° at ~1×10^4 Hz.

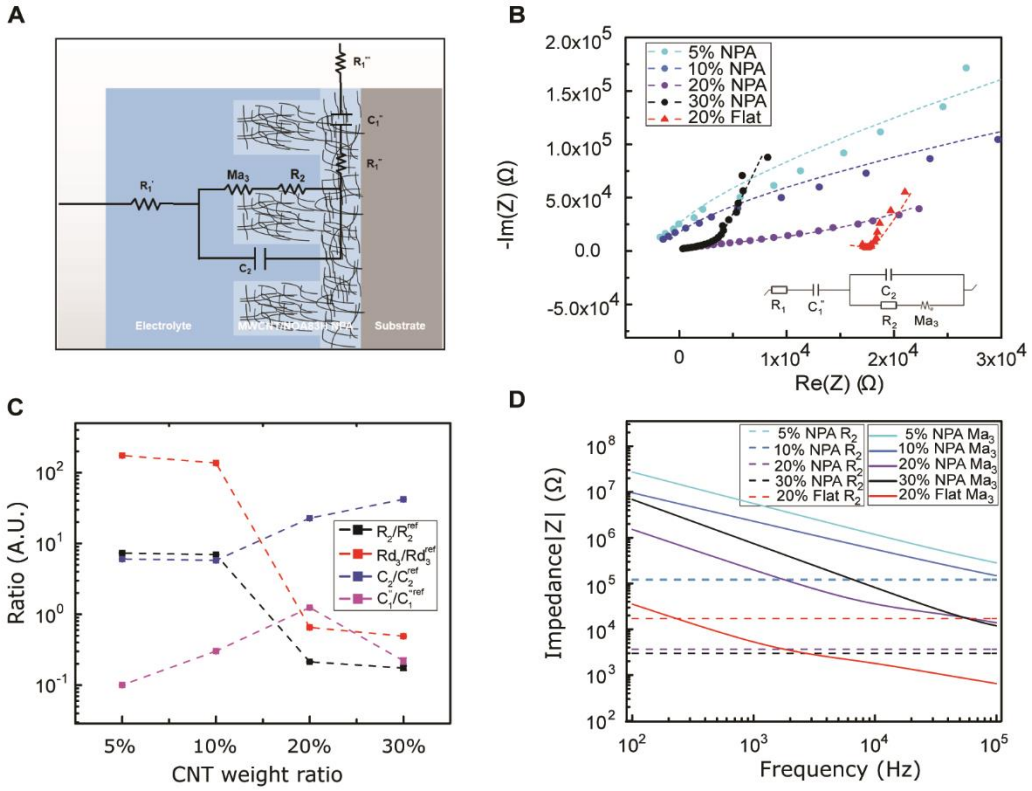

Figure 4. Analysis of different MWCNT ratio of conductive MWCNT/polymer composite. (A) Schematic equivalent circuit model. (B) Nyquist plots and equivalent circuit model of different MWCNT ratio and different structure of conductive MWCNT/polymer composite from 10^2 Hz to 10^5 Hz in pH=7.4 PBS solution. (C) The ratio plot of different fitting parameters to the conductive MWCNT/polymer flat composite reference for different MWCNT loading of conductive MWCNT/polymer composite. (D) The plot of R_2 and calculated Ma_s value of different MWCNT ratios and different structures of conductive MWCNT/polymer composite from 10^2 Hz to 10^5 Hz.

3.2.3 Analysis by equivalent circuit modeling

To better understand the effects of MWCNT ratios and nanostructured surface geometries on EIS properties, we conducted an equivalent circuit modeling to fit and analyze the measured Nyquist plots for different MWCNT/polymer samples. Figure 4A illustrates the equivalent circuit we used for fitting the EIS spectra, where R_1' is the electrolyte resistance, R_1'' is the bulk resistance of the MWCNT/polymer composite, R_1''' includes all parasitic contact resistance and equipment resistance in the circuit, C_1'' describes the bulk

capacitance of the MWCNT/polymer composite, R_2 is the charge transfer resistance at the interface between MWCNTs and electrolyte, C_2 is the double-layer capacitance at the interface between MWCNTs and the electrolyte, and Ma_3 is the anomalous diffusion impedance for ion diffusion at the interface between MWCNTs and the electrolyte. In particular, the anomalous diffusion of ions is mainly caused by the nanoscale porous structures at the interface between MWCNT/polymer composites and the electrolyte.[31, 32] The diffusion of ions in porous structure does not obey Fick's laws and thus cannot be modeled as a standard Warburg impedance term. By modifying Fick's equations and solving the differential equations under nanoporous boundary conditions, the anomalous diffusion impedance Ma_3 can be express as:[33]

$$Ma_3(j\omega) = Rd_3 * \left(\frac{\omega_d}{j\omega}\right)^{\frac{\alpha}{2}} * \coth\left[\left(\frac{j\omega}{\omega_d}\right)^{\frac{\alpha}{2}}\right] \quad (2),$$

$$\frac{2\pi}{\omega_d} = \frac{t^2}{D} \quad (3),$$

where Rd_3 is the anomalous diffusion impedance amplitude, j is the imaginary unit, ω is the frequency, ω_d is the characteristic angular frequency, α is the sub-diffusion parameter for describing the fractal geometry of nanoporous structures, t is the effective thickness of the nanoporous MWCNT/polymer layer for the anomalous diffusion, and D is the diffusion coefficient. The ion movement behaviors are very different between low-frequency and high-frequency limits. When ω is much larger than ω_d, the effective ion concentration at the electrode surface is not disturbed by AC electrical fields, reaching the chemical dynamics regime. When ω is much smaller than ω_d, the ion concentration at the electrode surface depends on the phase of AC electrical fields and the ion diffusion constant, reaching the diffusion regime.

Figure 4B depicts the Nyquist plots in the range between 10^3 and 10^5 Hz for different MWCNT/polymer samples. Based on the equivalent circuit modeling in Figure 4A, we used the randomization method to fit equivalent circuit elements and produced fitting curves (dash lines, Figure 4B) in good agreement with measurements (discrete dots, Figure 4B) for different samples. The randomization fitting methods start

with some initial parameter values and randomize them to minimize $\chi^2/|Z|$ in Ohm. $\chi^2/|Z|$ can be expressed as:[34]

$$\chi^2/|Z| = \frac{1}{n}\sum_{i=1}^{n}\frac{|Z_{meas}(i)-Z_{simul}(\omega_i param)|^2}{(Z_{meas}(i))} \quad (4),$$

where $Z_{meas}(i)$ is the measured impedance, and $Z_{simul}(\ _i, param)$ is the calculated value based on fitting parameters at different frequency $\ _i$. By examining the fitted values of the equivalent circuit elements in Table 1, we can have a mechanistic understanding of the difference of EIS properties between different samples. Since R_1'' resistance for the MWCNT/polymer sample is in series with the electrolyte resistance R_1' and the remaining parasitic circuit/contact resistance R_1''', R_1'' cannot be differentiated from R_1' *and* R_1''' in the fitting. Thus, the table does not include the circuit items for R_1', R_1'', *and* R_1'''.

As shown in Table 1, the 20 wt% MWCNT/polymer flat sample and the 20 wt% MWCNT/polymer nanopillar arrays share similar fitted values of anomalous diffusion impedance (including Rd_3, t_3, and $\ _3$) and the MWCNT network capacitance (C_1"), indicating their similar fractal nanoporous structures as well as similar distribution and density properties of MWCNT networks. However, 20 wt% MWCNT/polymer nanopillar arrays show much smaller values for both charge transfer resistance (R_2: ~3653) and double-layer capacitance (C_2: ~0.618 × 10^{-9} F) than the 20 wt% MWCNT/polymer flat sample (R_2: ~17127 C_2: ~2.712 × 10^{-11} F), reflecting the much larger active surface area to interact with the electrolyte environment in both Faradic and non-Faradic processes. The observation of very different R_2 and C_2 values between nanopillar array and flat samples of the same 20% MWCNT ratio suggests that the nanoimprinting process for creating nanopillar arrays may mechanically force more MWCNTs to penetrate out of their polymer matrix for direct interfacing with electrolytes. The impedance of a capacitor inversely depends on the frequency, and can be expressed as:

$$Z_c = \frac{1}{\omega C} j \quad (5),$$

$$C = \varepsilon \frac{A}{d} \quad (6),$$

where C is the capacitance, ε is the permittivity, A is the area of the two neighboring electrodes, and d is the distance between the two neighboring electrodes. For 20 wt% MWCNT/polymer flat sample, at 10^5 Hz, the $|Z_{C2}|$ calculated by Eq. (5) is 58946 Ω, the $|Ma_3|$ calculated by Eq. (2) is 649.94 . Therefore, $|Z_{C2}|$ is much larger than the summation of R_2 and $|Ma_3|$, which explains its frequency-insensitive impedance response between ~$3x10^3$ Hz and ~$1x10^5$ Hz (Figure 3B). In contrast, for 20 wt% MWCNT/polymer nanopillar arrays at 10^5 Hz, $|Z_{C2}|$ is 9705 , $|Ma_3|$ is 13882 , and R_2 is 3653 . Since $|Z_{C2}|$ is smaller than the summation of R_2 and $|Ma_3|$, the impedance for 20 wt% MWCNT/polymer nanopillar arrays continuously decreases with increasing frequency (Figure 3B).

To examine the effects of the MWCNT ratio on the electrochemical impedance properties of MWCNT/polymer nanopillar arrays, we used the 20 wt% MWCNT/polymer flat sample as a reference and plot the fitted ratiometric values of equivalent circuit elements for nanopillar arrays with different MWCNT ratios, including $C_1''/C_1''^{(ref)}$ for the MWCNT network capacitance, $C_2/C_2^{(ref)}$ for the double-layer capacitance, $R_2/R_2^{(ref)}$ for the charge transfer resistance, and $Rd_3/Rd_3^{(ref)}$ for the anomalous diffusion impedance. In Figure 4C, we can observe several key points. First, before reaching the percolation threshold, as the MWCNT ratio increases from 5 wt% to 10 wt%, $C_1''/C_1''^{(ref)}$ increases from 0.10 to 0.30 by ~3 times, $C_2/C_2^{(ref)}$ slightly increases from 6.05 to 5.79, $R_2/R_2''^{(ref)}$ slightly decreases from 7.32 to 6.97, and $Rd_3/Rd_3''^{(ref)}$ decreases from 174.70 to 137.35. Therefore, for the disconnected MWCNTs in the polymer matrix, the change of MWCNT ratios does not have a significant effect on the values for the circuit elements at the interface with electrolyte environments (e.g., C_2, R_2, and Rd_3); but the bulk capacitance C_1'' can still increase significantly with the MWCNT ratio due to an increased electrode surface area (A) of MWCNTs and a reduced mean distance (d) between MWCNTs in the MWCNT/polymer composite, described by Equation 6. Second, as the MWCNT ratio increases across the percolation threshold from 10 wt% to 20 wt%, $C_1''/C_1''^{(ref)}$ increases from 0.30 to 1.25, $C_2/C_2^{(ref)}$ increases from 5.8 to 22.8 by ~4 times, $R_2/R_2''^{(ref)}$ decreases from 6.97 to 0.21 by, and $Rd_3/Rd_3''^{(ref)}$ decreases from 137.4 to 0.65. In addition to the ~4 times increase of interfacial and bulk

capacitance C_1" and C_2, reaching the percolation threshold can lead to a ~35 times *drop of* R_2 and a ~210 times *drop of* Rd_3, which suggests that the charge transport and ion diffusion processes at the electrolyte interface strongly depends on the formation of interconnected MWCNT networks. Third, after going beyond the percolation threshold, as the MWCNT ratio further increases from 20% to 30%, $C_1"/C_1"^{(ref)}$ decreases from 1.25 to 0.22 by ~5.7 times, $C_2/C_2^{(ref)}$ increases from 22.78 to 42.07 by ~2 times, $R_2/R_2"^{(ref)}$ slightly decreases from 0.21 to 0.17, and $Rd_3/Rd_3"^{(ref)}$ slightly decreases from 0.65 to 0.49. The significant drop for the bulk capacitance C_1" and relatively small changes for interfacial circuit elements of C_2, R_2, and Rd_3 can be explained by the formation of MWCNT aggregations in the polymer matrix because of the poor dispersion of MWCNTs in the polymer matrix at very high MWCNT ratios (~30%).

To investigate the relative contributions to the interfacial impedance between charge transport term R_2 and ion diffusion term Ma_3, we compared the fitted impedance spectra for R_2 (solid curves, Figure 4D) and Ma_3 (solid curves, Figure 4D) for different samples. Unlike R_2 independent on the frequency changes, the impedance for Ma_3 decreases with the frequency following Equation (2). Compared to the 20% MWCNT/polymer flat sample, the 20% MWCNT/polymer nanopillar arrays show a ~45 times impedance increase for Ma_3 but a ~5 times impedance drop for R_2 over the entire frequency range between $10^2 – 10^5$ Hz (Figure 4D). The smaller R_2 for the nanopillar sample than the flat sample suggests that the mechanical forces during the nanostructured imprinting process can expose more electrochemical active MWCNTs on the surface of MWCNT/polymer nanopillar arrays in the electrolyte environment. On the other side, the much larger Ma_3 impedance for the nanopillar sample than the flat sample indicates that the nanoimprinting process can cause a higher degree of microscopic porosity on the surface of MWCNT/polymer nanopillar arrays to slow down the ion diffusion process at the interface with the electrolyte. For MWCNT/polymer nanopillar arrays with different MWCNT ratios, the impedance for Ma_3 is dominant over R_2 (Figure 4D), revealing a faster rate of the Faradic electron charge transport process than the ion diffusion process in the tested frequency range between $10^2 – 10^5$ Hz.

The presented EIS data is from one typical sample, but we measured at least three different areas for each sample and 3 samples for each processing condition(Figure. S-4, †). Three different areas from one sample EIS results demonstrate the sample's uniformity, while 3 different samples EIS results demonstrate our

fabrication method's reproducibility(Figure. S-5, †). Meanwhile, the fitting parameters are plotted (table S-2, †). More detailed discussion is in supplemental information.

Condition \ Circuit components	$\chi^{2}/\|Z\|$	R_2 (Ω)	Rd_3 (Ω)	Wd_3 (rad/s)	a_3 (a.u.)	C2 (nF)	C1″ (F)
20% flat	0.43	17127	3.43×10^{6}	0.061	0.999	2.712×10^{-2}	5.381
5% NPA	0.358	125428	5.94×10^{8}	0.050	0.989	0.164	0.541
10% NPA	0.267	119300	4.67×10^{8}	0.057	0.995	0.157	1.626
20% NPA	0.052	3654	2.22×10^{6}	0.070	0.806	0.618	6.716
30% NPA	0.031	3985	1.67×10^{6}	0.085	0.885	1.141	1.188

Table 1. Fitting parameters of different MWCNT ratio

3.3 Study of MWCNT/polymer nanopillar arrays with different annealing temperatures

3.3.1 Conductivity properties

We investigated the annealing effects on the electrical properties of 20 wt% MWCNT/polymer nanopillar arrays by 4-point probe measurements. As the annealing temperature increases from 130 ˚C to 200 ˚C and 300 ˚C, the conductivity of the sample increases from 3.58 S/m to 5.99 S/m and 6.41 S/m, with the relative standard deviation increased from 34.0% to 65.5% and 95.8% (Figure 5A). The observation of increased conductivity with the annealing temperature for MWCNT/polymer nanopillar arrays indicates that the connectivity of MWCNT networks in the polymer matrix can be increased by the annealing process. As suggested by the previous report,[35]·[36] with the annealing temperature above the polymer glass transition temperature, the nanoimprinting-stressed MWCNTs can experience self-relaxation and self-reorientation in the softened polymer matrix, which may reduce the mean distance among individual MWCNTs in the network to increase the conductivity of MWCNT networks. The increase of the relative standard deviation of measured conductivity with increased annealing temperature may be associated with the stochastic nature of self-relaxation and self-reorientation processes of MWCNT networks, which are ununiformly distributed in the

polymer matrix. Notably, we have observed that the nanopillar structure of MWCNT/polymer can vanish at the annealing temperature above 400˚C.

3.3.2 EIS properties

Figure 5B shows that MWCNT/polymer nanopillar arrays treated at a higher annealing temperature possess a lower impedance over the tested frequency range between 10^2 – 10^5 Hz. At 1000 Hz, as the annealing temperature increases from 130 ˚C to 200 ˚C and 300 ˚C, the impedance drops from $4.5x10^4$ Ω to $1.5\ x10^4$ Ω and $7.9x10^3$ Ω, which agrees with the decreasing trend of measured DC conductivity (Figure 5A). As shown in Figure 5C, conductive nanopillar arrays with different annealing temperatures reveal a similar profile for measured spectra of impedance phase angle, which first increases and then decreases with frequency, reaching a peak value between 10^3 Hz and 10^4 Hz.

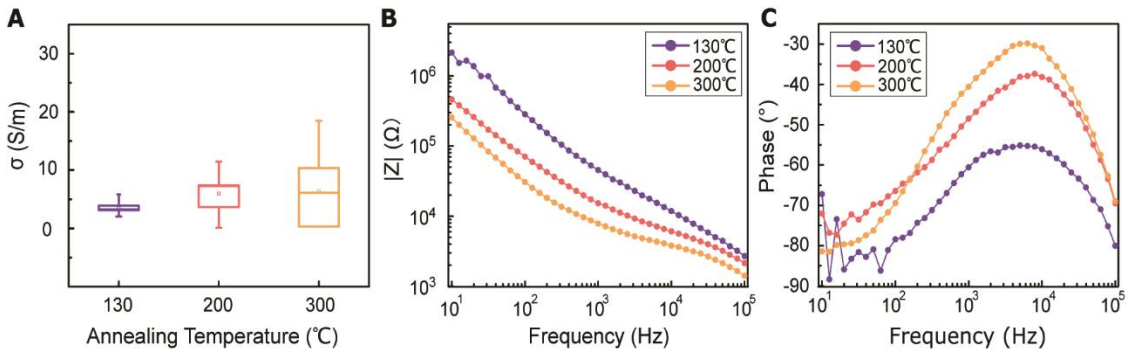

Figure 5. Conductivity and EIS characterization of annealing effect on 20 wt% conductive MWCNT/polymer composite NPAs. (A) Results of conductivity of 20 points per sample calculated from the sheet resistance measured by 4 point probe of annealing effect on 20 wt% conductive MWCNT/polymer composite. (B,C) EIS (B) impedance and (C) phase results of different annealing effect on 20 wt% conductive MWCNT/polymer composite from 10^1 Hz to 10^5 Hz in pH=7.4 PBS solution.

3.3.3 Analysis by equivalent circuit modeling

To understand the EIS properties of MWCNT/polymer nanopillar arrays under different annealing temperatures, we conducted the equivalent circuit modeling (Figure 4A) to fit the measured curves in the

Nyquist plot (Figure 6A). Table 2 illustrates the fitted parameters of the circuit elements for different samples. By using the 20 wt% MWCNT/polymer flat sample as a reference, we plotted the ratiometric values of $C_1''/C_1''^{(ref)}$, $C_2/C_2^{(ref)}$, $R_2/R_2^{(ref)}$, and $Rd_3/Rd_3^{(ref)}$ for 20 wt% MWCNT/polymer nanopillar arrays with different annealing temperatures (Figure 6B).

As the annealing temperature increases from 130 ˚C to 200 ˚C, $C_1''/ C_1''^{(ref)}$ increases by ~5 times from 1.25 to 7.51, $Rd_3/Rd_3''^{(ref)}$ decreases from 0.65 to 0.46, $C_2/C_2^{(ref)}$ slightly increases from 22.79 to 25.40, and $R_2/R_2''^{(ref)}$ slightly changes from 0.21 to 0.20 (Figure 6B). The significant increase of the bulk capacitance term $C_1''/ C_1''^{(ref)}$ indicates a reduced mean distance (*d*) between individual MWCNTs due to the self-relaxation and self-reorientation of MWCNTs in the softened polymer matrix at 200 ˚C, which agrees with the observation of increased conductivity from 4-probe measurements (Figure 5A). The decrease of the anomalous diffusion term $Rd_3/Rd_3''^{(ref)}$ suggests a reduced nanoscale porosity at the interface between MWCNT/polymer nanopillar arrays and the electrolyte due to the annealing. The small changes of the double-layer capacitance term $C_2/C_2^{(ref)}$, and charge transport resistance term $R_2/R_2''^{(ref)}$ indicates the density of the interfacial MWCNTs exposed to the electrolyte does not change much with the annealing temperature increased from 130 ˚C to 200 ˚C.

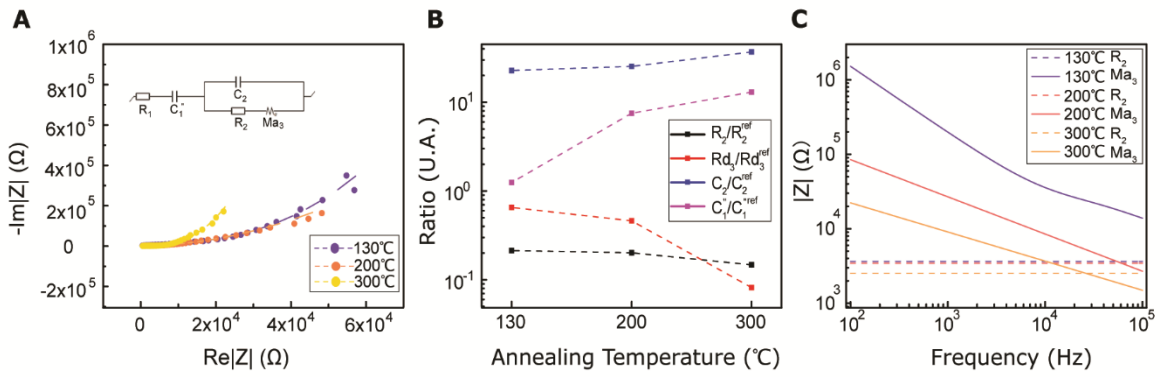

Figure 6. Analysis of the annealing effect on conductive MWCNT/polymer composite NPAs. (A) Nyquist plots and equivalent circuit model of different annealing temperature on conductive MWCNT/polymer composite NPAs from 10^2 Hz to 10^5 Hz. (B) The ratio plot of different fitting parameters to the conductive MWCNT/polymer flat composite reference for different annealing temperatures on conductive MWCNT/polymer composite NPAs. (D) The plot of R_2 and calculated Ma_s value of different annealing temperature on conductive MWCNT/polymer composite NPAs from 10^2 Hz to 10^5 Hz.

As the annealing temperature further increases from 200 ˚C to 300 ˚C, C_1''/ C_1''$^{(ref)}$ increases from 7.51 to 13.02, Rd_3/Rd_3''$^{(ref)}$ decreases by ~6 times from 0.46 to 0.08, $C_2/C_2^{(ref)}$ increases from 25.40 to 36.87, and R_2/R_2''$^{(ref)}$ decreases from 0.20 to 0.15 (Figure 6B). Therefore, by using an even higher annealing temperature at 300 ˚C, the mean distance between individual MWCNTs can further be decreased to increase the bulk capacitance term C_1''/ C_1''$^{(ref)}$, and the nanoscale porosity can also be reduced to decrease the ion diffusion impedance Rd_3/Rd_3''$^{(ref)}$. Furthermore, the significant increase of the double-layer capacitance term $C_2/C_2^{(ref)}$ *and* non-negligible decrease of charge transport resistance term R_2/R_2''$^{(ref)}$ suggests an increased density of the interfacial MWCNTs exposed to the electrolyte, which may be due to the heat-induced rearrangement of the interfacial MWCNTs on the surface of MWCNT/polymer nanopillar arrays.

Condition \ Circuit components	$\chi^2/\|Z\|$	R_2 (Ω)	Rd_3 (Ω)	Wd_3 (rad/s)	a_3 (a.u.)	C2 (nF)	C1″ (F)
20% NPA 0 °C	0.052	3653	2.22×10^6	0.070	0.806	0.618	6.716
20% NPA 200 °C	0.035	3451	1.57×10^6	0.145	0.792	0.683	40.43
20% NPA 300 °C	0.032	2525	2.78×10^5	0.995	0.782	1.032	70.08

Table 2. Fitting parameters of different MWCNT ratio at different temperature

Figure 6C compares the interfacial impedance contributions due to the charge transport term R_2 and the anomalous ion diffusion term Ma_3 for MWCNT/polymer nanopillar arrays with different annealing temperatures. First, by increasing the annealing temperature from 130 ˚C to 200 ˚C and 300 ˚C, the impedance for anomalous ion diffusion Ma_3 can decrease almost by 2 orders of magnitude in the frequency range between $10^2 – 10^5$ Hz, while the charge transport resistance R_2 decreases by a much smaller factor. Second, although the impedance for Ma_3 is dominant over R_2 in the frequency range below 10^4 Hz, the difference of the impedance values between Ma_3 and R_2 can be significantly reduced by the annealing process at 300 ˚C. Therefore, a proper annealing process can help to reduce the overall impedance of MWCNT/polymer nanopillar arrays in (1) the bulk contributions from the resistance R_1" and capacitance C_1" terms of MWCNT networks by softening the polymer matrix and reducing the mean distance between MWCNTs, (2) as well as the interfacial contributions from the anomalous ion diffusion Ma_3 and charge transport R_2 terms by smoothing the nanoporous structures and increasing the MWCNT densities exposed to the electrolyte.

3.4 Additional results

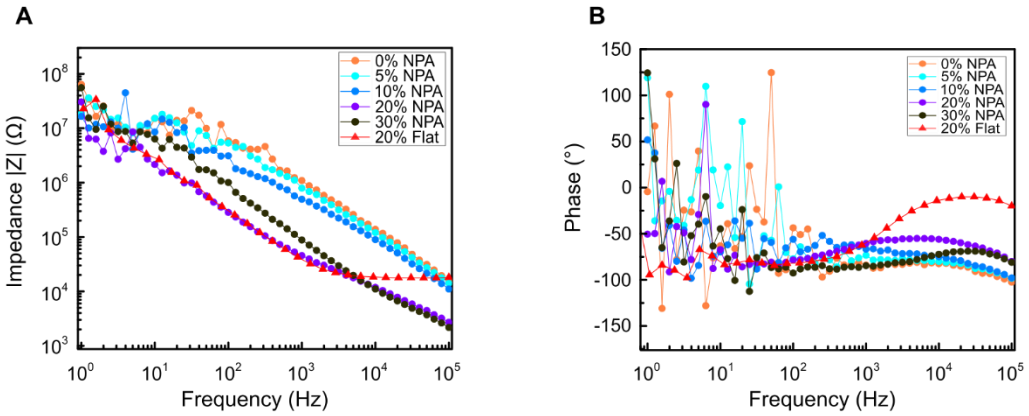

Figure S-2. Full range results of EIS measurement. (A) Impedance and (B) phase results of different MWCNT ratios and different structures of conductive MWCNT/polymer composite.

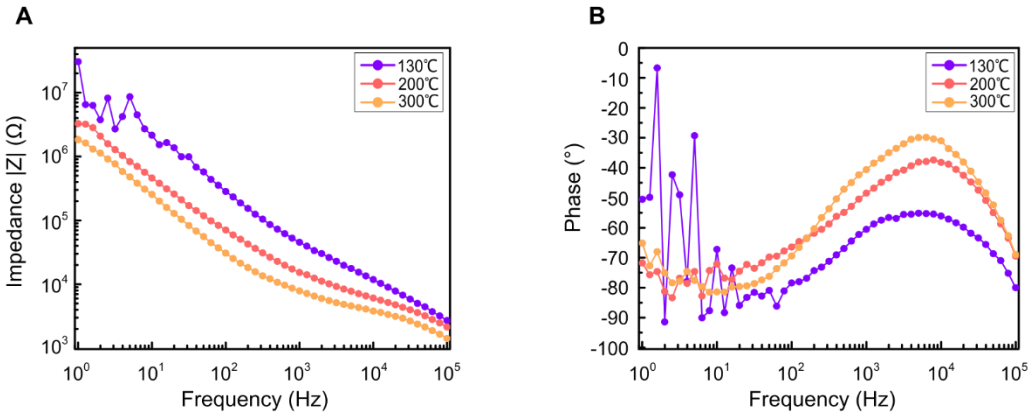

Figure S-3. Full range results of EIS measurement of annealing effect. (A) Impedance and (B) phase results of the annealing effect on 20 wt% conductive MWCNT/polymer composite NPAs.

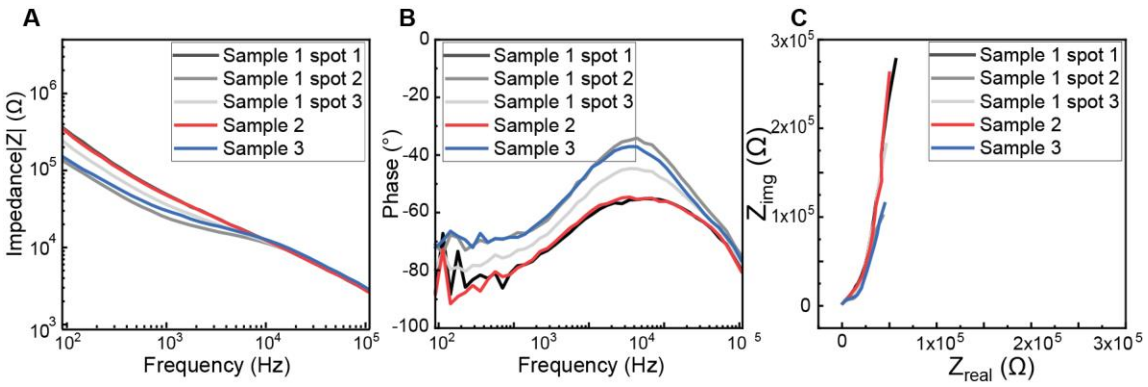

Figure S-4. EIS results from 3 different areas of 1 sample and 3 different samples. EIS measured (A) bode impedance |Z|, (B) bode phase angle and (C) Nyquist impedance plot for 20% MWCNT/polymer nanopillar arrays with 3 different areas from 1 sample and 3 different samples in 1X PBS (pH=7.4) in the frequency range from 10^2 Hz to 10^5 Hz.

The presented Electrochemical impedance spectrum (EIS) data is from one typical sample, but we measured at least three different areas for each sample and 3 samples for each processing condition.

We plotted the EIS results of three different areas from one sample and three different samples by bode plot and Nyquist plot (Figure S-4). Three different areas from one sample EIS results demonstrate the sample's uniformity, while three different samples EIS results demonstrate our fabrication method's reproducibility. Figure S-4A shows the impedance of all conditions in a similar range and similar trend, which starts from 10^5 Ω range and decreases to 10^3 Ω range when frequency increases from 10^2 Hz to 10^5 Hz. Meanwhile, figure S-4B shows that even the phase of all conditions has different values; they all follow a similar trend that increases first from ~-80° to -50° as frequency increase from 10^2 Hz to 10^4 Hz then starts to decrease back to -80° as the frequency further increases to 10^5 Hz. Figure S-4C further supports the phase change difference and the impedance |Z| difference at the low-frequency range. Different spots and different samples have similar real parts, while the imaginary part causes the difference in phase and impedance |Z|. The difference imaginary part value can be explained by the area-to-area difference and the sample-to-sample difference of the MWCNT network condition. However, the difference of the imaginary part is in the same

order, and the impedance |Z| are in the same order, which is very common in the fabrication of nanostructured substrates.

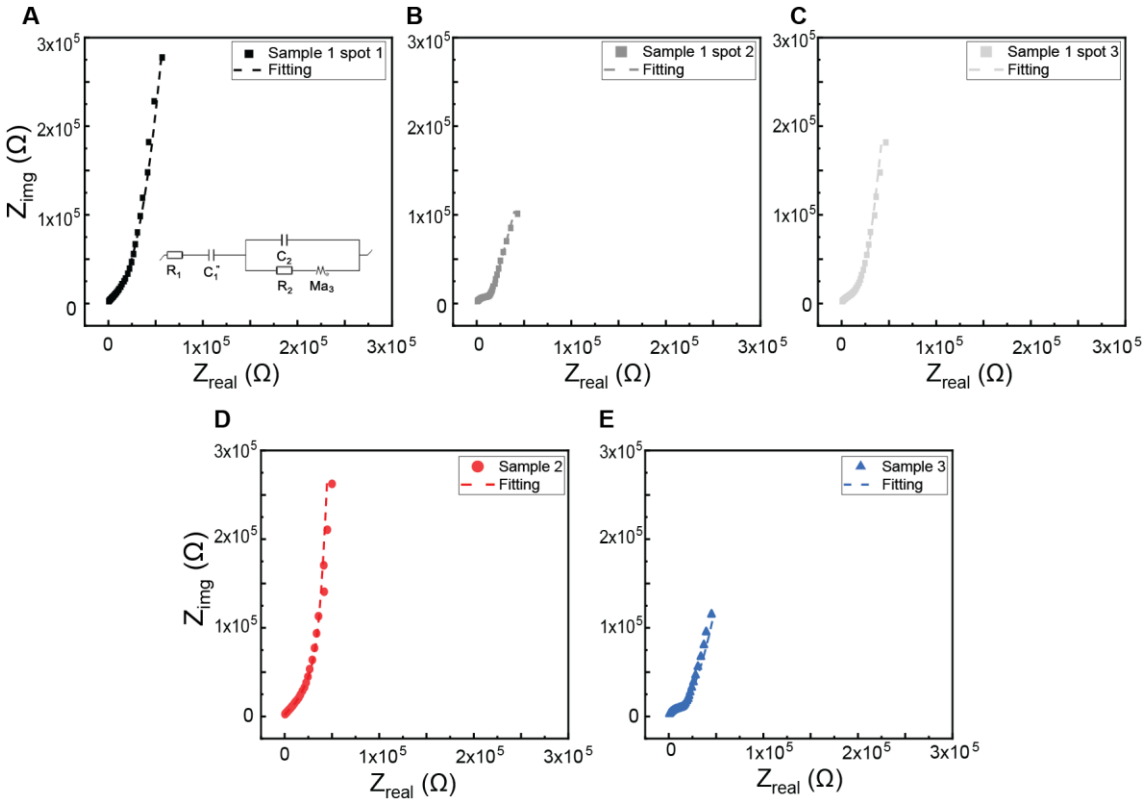

Figure S-5. Nyquist plots of different conditions and fitting with the same equivalent circuit model. Nyquist plot and fitting results for (A) spot 1, (B) spot2, (C) spot 3 on sample 1, (D) sample2, and (E) sample 3 in 1X PBS (pH=7.4) in the frequency range from 10^2 Hz to 10^5 Hz.

Condition \ Circuit components	$\chi^2/\|Z\|$	R_2 (Ω)	Rd_3 (Ω)	Wd_3 (rad/s)	a_3 (a.u.)	C2 (nF)	C1'' (F)
Spot1 sample 1	0.0038	3928	69589	0.4328	0.822	6.8	0.61
Spot 2 sample 1	0.0221	4665	85904	0.2845	0.839	1.6	0.54
Spot 3 sample 1	0.0094	4389	73421	0.3965	0.854	8.0	0.58
Sample 2	0.0398	4448	97763	0.2532	0.890	7.4	0.61
Sample 3	0.0771	4809	73680	0.4043	0.968	21.1	0.59

Table S-2. Table of fitting circuit parameters of different conditions.

We have plotted the Nyquist EIS results with fitting results using the same equivalent circuit model in the main manuscript (Figure S-2) and list them in a table to compare (Table S-2). From figure S-5, we can tell that the fitting is matching the experiment results, and this is further confirmed by the small $\chi^2/|Z|$ values listed in table S-2. By comparing all the fitting parameters in table S-2, we find out that all the parameters are in the same range. This similarity proves the good uniformity and reproducibility of our fabrication method of the conducting NPA made of MWCNT/polymer nanocomposites.

Chapter 4

4. Conclusion

In summary, we have developed a scalable, low cost, and high throughput nanoimprinting fabrication process to manufacture conducting MWCNT/polymer nanopillar arrays over the wafer-scale on both rigid and flexible substrates. We have conducted a systematic study to characterize and understand the dependence of the electrical properties of MWCNT/polymer nanopillar arrays on the MWCNT ratios and the annealing temperatures in the fabrication process. In particular, we find that both charge transport resistance and anomalous ion diffusion impedance at the electrolyte interface can decrease dramatically by increasing the MWCNT ratio over the percolation threshold to form interconnected MWCNT networks. Furthermore, we observe that MWCNT/polymer nanopillar arrays treated with an annealing temperature at 200 and 300 ˚C can have increased bulk conductivity, increased bulk capacitance, and reduced interfacial anomalous ion diffusion impedance. Compared to most nanopillar arrays made of inorganic conducting materials (e.g., Si, Au, and Pt) by conventional nanoengineering, nanoimprinting fabricated conducting MWCNT/polymer nanopillar arrays have unique advantages, such as combined mechanical flexibility and strength, roll-to-toll manufacturing scalability, and fabrication compatibility with both rigid and flexible substrates. Therefore, we envision that conducting MWCNT/polymer nanopillar arrays by scalable nanoimprinting fabrication can open new opportunities in flexible wearable sensing devices, flexible implantable biosensors, and low-cost disposable biochips. Toward the use of conducting MWCNT/polymer nanopillar arrays for bioelectrical recording and electrochemical sensing, future research can explore the methods (1) for further improvement of the local dispersion uniformity of MWCNT networks in uncured polymer materials, and (2) for scalable patterning, metallization, lift-off, and passivation processes to create many individually addressable recording sites composed of MWCNT/polymer nanopillar arrays.

References

[1] L. Hanson, Z. C. Lin, C. Xie, Y. Cui, and B. X. Cui, "Characterization of the Cell-Nanopillar Interface by Transmission Electron Microscopy," *Nano Letters,* vol. 12, no. 11, pp. 5815-5820, Nov, 2012.

[2] J. T. Robinson, M. Jorgolli, A. K. Shalek, M. H. Yoon, R. S. Gertner, and H. Park, "Vertical nanowire electrode arrays as a scalable platform for intracellular interfacing to neuronal circuits," *Nature Nanotechnology,* vol. 7, no. 3, pp. 180-184, Mar, 2012.

[3] C. Xie, Z. L. Lin, L. Hanson, Y. Cui, and B. X. Cui, "Intracellular recording of action potentials by nanopillar electroporation," *Nature Nanotechnology,* vol. 7, no. 3, pp. 185-190, Mar, 2012.

[4] Z. L. C. Lin, C. Xie, Y. Osakada, Y. Cui, and B. X. Cui, "Iridium oxide nanotube electrodes for sensitive and prolonged intracellular measurement of action potentials," *Nature Communications,* vol. 5, Feb, 2014.

[5] J. Abbott, T. Y. Ye, L. Qin, M. Jorgolli, R. S. Gertner, D. Ham, and H. Park, "CMOS nanoelectrode array for all-electrical intracellular electrophysiological imaging," *Nature Nanotechnology,* vol. 12, no. 5, pp. 460-466, May, 2017.

[6] C. Shin, W. Shin, and H. G. Hong, "Electrochemical fabrication and electrocatalytic characteristics studies of gold nanopillar array electrode (AuNPE) for development of a novel electrochemical sensor," *Electrochimica Acta,* vol. 53, no. 2, pp. 720-728, Dec 1, 2007.

[7] F. J. Rawson, M. T. Cole, J. M. Hicks, J. W. Aylott, W. I. Milne, C. M. Collins, S. K. Jackson, N. J. Silman, and P. M. Mendes, "Electrochemical communication with the inside of cells using micro-patterned vertical carbon nanofibre electrodes," *Scientific Reports,* vol. 6, Dec 1, 2016.

[8] M. Yang, S. B. Hong, J. H. Yoon, D. S. Kim, S. W. Jeong, D. E. Yoo, T. J. Lee, K. G. Lee, S. J. Lee, and B. G. Choi, "Fabrication of Flexible, Redoxable, and Conductive Nanopillar Arrays with Enhanced Electrochemical Performance," *Acs Applied Materials & Interfaces,* vol. 8, no. 34, pp. 22220-22226, Aug 31, 2016.

[9] C. Lotwala, and H. F. Ji, "Electrochemistry on nanopillared electrodes," *Aims Materials Science,* vol. 4, no. 2, pp. 292-301, 2017.

[10] W. T. Zhao, L. Hanson, H. Y. Lou, M. Akamatsu, P. D. Chowdary, F. Santoro, J. R. Marks, A. Grassart, D. G. Drubin, Y. Cui, and B. X. Cui, "Nanoscale manipulation of membrane curvature for probing endocytosis in live cells," *Nature Nanotechnology,* vol. 12, no. 8, pp. 750-+, Aug, 2017.

[11] H. Y. Lou, W. T. Zhao, Y. P. Zeng, and B. X. Cui, “The Role of Membrane Curvature in Nanoscale Topography-Induced Intracellular Signaling,” *Accounts of Chemical Research,* vol. 51, no. 5, pp. 1046-1053, May, 2018.

[12] J. T. Robinson, M. Jorgolli, A. K. Shalek, M.-H. Yoon, R. S. Gertner, and H. Park, “Vertical nanowire electrode arrays as a scalable platform for intracellular interfacing to neuronal circuits,” *Nature Nanotechnology,* vol. 7, no. 3, pp. 180-184, 2012.

[13] K. J. Byeon, and H. Lee, “Recent progress in direct patterning technologies based on nano-imprint lithography,” *The European Physical Journal - Applied Physics,* vol. 59, no. 1, pp. 10001, 2012.

[14] L. J. Guo, “Nanoimprint lithography: Methods and material requirements,” *Advanced Materials,* vol. 19, no. 4, pp. 495-513, Feb 19, 2007.

[15] M. C. Traub, W. Longsine, and V. N. Truskett, “Advances in Nanoimprint Lithography,” *Annual Review of Chemical and Biomolecular Engineering, Vol 7,* vol. 7, pp. 583-604, 2016.

[16] J. Yu, K. Lu, E. Sourty, N. Grossiord, C. E. Koning, and J. Loos, “Characterization of conductive multiwall carbon nanotube/polystyrene composites prepared by latex technology,” *Carbon,* vol. 45, no. 15, pp. 2897-2903, 2007/12/01/, 2007.

[17] "Polymer Nanotube Nanocomposites: A Review of Synthesis Methods, Properties and Applications," *Polymer Nanotube Nanocomposites*, pp. 1-44.

[18] T. D. Prichard, S. S. Singh, N. Chawla, and B. D. Vogt, “Flocculated carbon nanotube composites for solvent resistant soft templated microfeatures,” *Polymer,* vol. 54, no. 3, pp. 1130-1135, 2013/02/05/, 2013.

[19] S. Kundu, Y. Wang, W. Xia, and M. Muhler, “Thermal Stability and Reducibility of Oxygen-Containing Functional Groups on Multiwalled Carbon Nanotube Surfaces: A Quantitative High-Resolution XPS and TPD/TPR Study,” *The Journal of Physical Chemistry C,* vol. 112, no. 43, pp. 16869-16878, 2008/10/30, 2008.

[20] Y. Guo, K. Ruan, X. Yang, T. Ma, J. Kong, N. Wu, J. Zhang, J. Gu, and Z. Guo, “Constructing fully carbon-based fillers with a hierarchical structure to fabricate highly thermally conductive polyimide nanocomposites,” *Journal of Materials Chemistry C,* vol. 7, no. 23, pp. 7035-7044, 2019.

[21] A. Forcellese, M. Simoncini, A. Vita, A. Giovannelli, and L. Leonardi, “Performance analysis of MWCNT/Epoxy composites produced by CRTM,” *Journal of Materials Processing Technology,* vol. 286,

pp. 116839, 2020/12/01/, 2020.

[22] M. Kumar, J. S. Saini, and H. Bhunia, “Performance of Mechanical Joints Prepared from Carbon-Fiber-Reinforced Polymer Nanocomposites under Accelerated Environmental Aging,” *Journal of Materials Engineering and Performance*, 2020/10/28, 2020.

[23] J. Henzie, M. H. Lee, and T. W. Odom, “Multiscale patterning of plasmonic metamaterials,” *Nat Nanotechnol,* vol. 2, no. 9, pp. 549-54, Sep, 2007.

[24] B. Bhushan, D. Hansford, and K. K. Lee, “Surface modification of silicon and polydimethylsiloxane surfaces with vapor-phase-deposited ultrathin fluorosilane films for biomedical nanodevices,” *Journal of Vacuum Science & Technology A,* vol. 24, no. 4, pp. 1197-1202, 2006.

[25] B. Technology. "Four Point Probe Equations," http://four-point-probes.com/four-point-probe-equations/.

[26] E. P. Dupont, R. Luisier, and M. A. M. Gijs, “NOA 63 as a UV-curable material for fabrication of microfluidic channels with native hydrophilicity,” *Microelectronic Engineering,* vol. 87, no. 5, pp. 1253-1255, 2010/05/01/, 2010.

[27] D. Qin, Y. Xia, and G. M. Whitesides, “Soft lithography for micro- and nanoscale patterning,” *Nature Protocols,* vol. 5, pp. 491, 02/18/online, 2010.

[28] J.-D. Cho, D.-P. Kim, and J.-W. Hong, “Photocuring Behaviors of UV-Curable Perfluoropolyether-Based Fluoropolymers with and without Tertiary Amine,” *Open Journal of Organic Polymer Materials,* vol. Vol.04No.01, pp. 4, 2014.

[29] L. Bokobza, and J. Zhang, “Raman spectroscopic characterization of multiwall carbon nanotubes and of composites,” *Express Polymer Letters,* vol. 6, no. 7, pp. 601 - 608, 2012-07-02, 2012.

[30] F. Du, J. E. Fischer, and K. I. Winey, “Effect of nanotube alignment on percolation conductivity in carbon nanotube/polymer composites,” *Physical Review B,* vol. 72, no. 12, pp. 121404, 09/19/, 2005.

[31] Z. Pomerantz, G. Garcia-Belmonte, A. Joseph, J.-P. Lellouche, J. Bisquert, and A. Zaban, “The effect of ion-polymer binding on ionic diffusion in dicarbazole-based conducting polymers,” *Electrochimica Acta,* vol. 52, no. 24, pp. 6841-6847, 2007.

[32] S. A. Tali, S. Soleimani-Amiri, Z. Sanaee, and S. Mohajerzadeh, “Nitrogen-doped amorphous carbon-silicon core-shell structures for high-power supercapacitor electrodes,” *Sci Rep,* vol. 7, pp. 42425, Feb 10, 2017.

[33] J. Bisquert, and A. Compte, “Theory of the electrochemical impedance of anomalous diffusion,” *Journal of Electroanalytical Chemistry*, vol. 499, no. 1, pp. 112-120, 2001/02/23/, 2001.

[34] B. s. instuments, "EC-Lab software analysis and data process," 2018].

[35] B. H. Cipriano, A. K. Kota, A. L. Gershon, C. J. Laskowski, T. Kashiwagi, H. A. Bruck, and S. R. Raghavan, "Conductivity enhancement of carbon nanotube and nanofiber-based polymer nanocomposites by melt annealing," *Polymer*, 22, 2008, pp. 4846-4851.

[36] H. Deng, T. Skipa, R. Zhang, D. Lellinger, E. Bilotti, I. Alig, and T. Peijs, “Effect of melting and crystallization on the conductive network in conductive polymer composites,” *Polymer,* vol. 50, no. 15, pp. 3747-3754, 2009/07/17/, 2009.